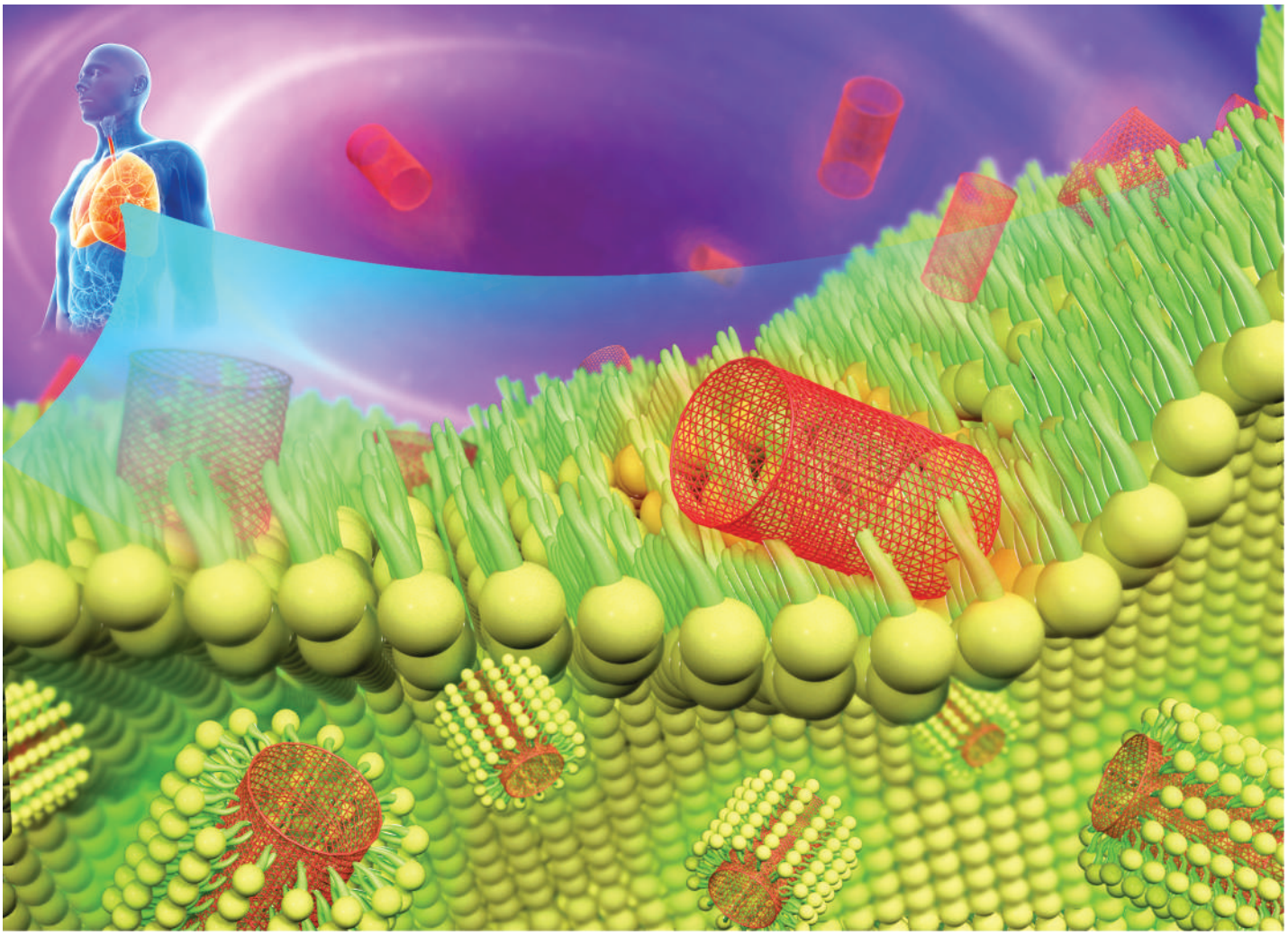

Showcasing research from State Key Laboratory of Heavy Oil Processing, Center for Bioengineering and Biotechnology, College of Chemical Engineering, China University of Petroleum (East China), Qingdao, China.

Perturbation of the pulmonary surfactant monolayer by single-walled carbon nanotubes: a molecular dynamics study

The large scale synthesis of single-walled carbon nanotubes (SWCNTs) has put human health at high risk. In this work, by using the molecular dynamics simulation method, how the diameter and length of inhaled SWCNTs critically regulate their interactions with the pulmonary surfactant monolayer was demonstrated. These advanced results could help reveal the inhalation toxicity of SWCNTs, and pave the way for the safe use of SWCNTs as vehicles for pulmonary drug delivery.

As featured in:

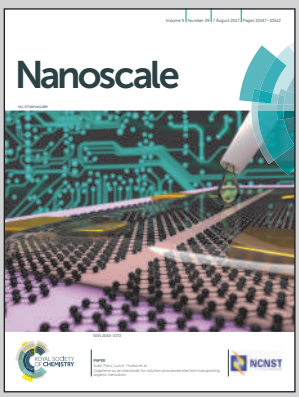

See Tongtao Yue *et al.*, *Nanoscale*, 2017, **9**, 10193.

ROYAL SOCIETY OF CHEMISTRY

rsc.li/nanoscale

Registered charity number: 207890

Nanoscale

PAPER

View Article Online
View Journal | View Issue

Cite this: *Nanoscale*, 2017, **9**, 10193

Perturbation of the pulmonary surfactant monolayer by single-walled carbon nanotubes: a molecular dynamics study†

Yan Xu,[a] Zhen Luo,[a] Shixin Li,[a] Weiguo Li,[b] Xianren Zhang,[c] Yi Y. Zuo,[d] Fang Huang[a] and Tongtao Yue *[a]

Single-walled carbon nanotubes (SWCNTs) are at present synthesized on a large scale with a variety of applications. The increasing likelihood of exposure to SWCNTs, however, puts human health at a high risk. As the front line of the innate host defense system, the pulmonary surfactant monolayer (PSM) at the air–water interface of the lungs interacts with the inhaled SWCNTs, which in turn inevitably perturb the ultrastructure of the PSM and affect its biophysical functions. Here, using molecular dynamics simulations, we demonstrate how the diameter and length of SWCNTs critically regulate their interactions with the PSM. Compared to their diameters, the inhalation toxicity of SWCNTs was found to be largely affected by their lengths. Short SWCNTs with lengths comparable to the monolayer thickness are found to vertically insert into the PSM with no indication of translocation, possibly leading to accumulation of SWCNTs in the PSM with prolonged retention and increased inflammation potentials. The perturbation also comes from the forming water pores across the PSM. Longer SWCNTs are found to horizontally insert into the PSM during inspiration, and they can be wrapped by the PSM during deep expiration *via* a tube diameter-dependent self-rotation. The potential toxicity of longer SWCNTs comes from severe lipid depletion and the PSM-rigidifying effect. Our findings could help reveal the inhalation toxicity of SWCNTs, and pave the way for the safe use of SWCNTs as vehicles for pulmonary drug delivery.

Received 7th February 2017,
Accepted 21st April 2017

DOI: 10.1039/c7nr00890b

rsc.li/nanoscale

Introduction

Single-walled carbon nanotubes (SWCNTs) display a number of unique properties which render them with potential applications in different areas of science and technology.[1] Currently, the worldwide production of SWCNTs is on the scale of several thousands of tons per year.[2] The ever-increasing demand for SWCNTs, however, increases the risk of human inhalation, especially for people who work with them.[3–5] On the positive side, SWCNTs have been used in biomedicine,[6–9] such as biomedical imaging[10] and drug delivery.[11–13]

SWCNTs have been investigated in the past few decades from the aspects of reducing the toxicity and promoting biomedical applications,[14–18] both of which require a systematic understanding of the interaction between SWCNTs and a variety of biomolecules.[19,20] The intensive study of SWCNT–membrane interaction provides information on both cell internalization and perturbation on cell membranes.[21–27] In addition, interacting with SWCNTs may change both the structure and activity of proteins.[28,29] Both the size and surface properties of SWCNTs were found to be important in affecting their interactions with biomolecules.[23,27,30]

Among all possible portals, the human lung can be easily accessed by SWCNTs due to its specific properties, *e.g.*, its thin epithelial barrier and large surface area.[31] Recently, SWCNTs were discovered in the bronchoalveolar lavage of asthmatic children.[32] Once inhaled, a large portion of the SWCNTs can reach the alveolar surface. The air–water interface of alveoli is covered by a thin pulmonary surfactant monolayer (PSM). The composition of the PSM is quite complex. Besides lipids that account for 90% of the pulmonary surfactant, proteins make up the other 10%.[33,34] For lipids, the most abundant com-

[a]*State Key Laboratory of Heavy Oil Processing, Center for Bioengineering and Biotechnology, College of Chemical Engineering, China University of Petroleum (East China), Qingdao 266580, China. E-mail: yuett@upc.edu.cn*
[b]*College of Science, China University of Petroleum (East China), Qingdao 266580, China*
[c]*State Key Laboratory of Organic-Inorganic Composites, Beijing University of Chemical Technology, Beijing 100029, China*
[d]*Department of Mechanical Engineering, University of Hawaii at Monoa, Honolulu, Hawaii 96822, USA*

†Electronic supplementary information (ESI) available: Initial configuration, additional simulation results, and five simulation videos. See DOI: 10.1039/c7nr00890b

ponent is dipalmitoylphosphatidylcholine (DPPC) along with a few others: phosphatidylcholine, phosphatidylglycerol and cholesterol.[35] Four kinds of proteins, including SP-A, SP-B, SP-C and SP-D, are associated with the pulmonary surfactant.[36,37] The major role of PSM is to reduce the surface tension of the alveolar air–water interface to prevent alveolar collapse during breathing and to modulate the innate immune defense.[38]

Like other nanoparticles,[39–44] inhaled SWCNTs are supposed to be able to translocate across the PSM. Concurrently, both the ultrastructure and mechanical properties of the PSM could be perturbed by the SWCNTs,[45] leading to toxicological effects, such as inflammation, conditions similar to asthma and respiratory distress syndrome.[46–48] As a common type of C-allotrope found in the atmosphere, fullerenes were found to rapidly aggregate in water but disaggregate after entering the membrane interior.[49] Once deposited on the PSM, differently, they were found to promote PSM collapse by reducing the mechanical rigidity.[43] By forming aggregates in the PSM, both the structural and mechanical properties of the PSM would be perturbed, thus causing fullerene toxicity.[42,50] Therefore, a thorough understanding of how the inhaled SWCNTs disrupt PSM is of great importance for developing effective strategies against the adverse effects of SWCNTs. Furthermore, the rational design of SWCNT-based pulmonary drug delivery requires a deep understanding of their translocation with both high efficiency and low toxicity. However, it is still difficult for the current experimental technologies to systematically probe and visualize the whole process of translocation and the accompanying PSM perturbation. Molecular dynamics simulation, on the contrary, can provide useful insights into the molecular mechanism of the interaction.[51] Here we present the first simulation study on SWCNT–PSM interaction, aiming at systematically studying the underlying mechanism of both PSM perturbation and translocation of inhaled SWCNTs.

Model and simulation method

System setup

Our simulation setup consists of two symmetric monolayers (PSMs) confining a water slab (Fig. S1†).[52] Each PSM is represented by a pure lipid monolayer, which is composed of 5102 DPPC molecules (Fig. S1a†). The DPPC model, taken from the Martini force field, is constructed by connecting a head group of four hydrophilic heads to two tails, each containing four hydrophobic beads (Fig. S1b†). The choice of DPPC was made because it is the major component of PSM which is responsible for reducing surface tension in the lungs to nearly zero.[53] Besides, a number of simulations have used the DPPC monolayer as a model PSM to investigate its interactions with nanoparticles.[40–42,44,50,54,55] In the coarse grained (CG) model, the honeycomb atomic structure of the SWCNT was reduced to a triangular lattice of the C1-type beads, where every three carbons in the all-atom (AA) SWCNT were modeled as one particle (Fig. S1c†). The angular force constant and the equilibrium angle along the axial direction are κ_{angle} = 700 kcal mol^{-1} rad^{-2} and θ = 60°, respectively. Along the radial direction, the equilibrium angle is not constant but determined by the tube diameter. The bond force constant and the equilibrium bond length are κ_{bond} = 700 kcal mol^{-1} and l = 0.3684 nm. The dihedral angle force constant, multiplicity and equilibrium angle are κ_{χ} = 3.1 kcal mol^{-1}, n = 2 and δ = 180°, respectively. The specific CG model was developed by Titov *et al.*,[56] and has been successfully used to simulate interactions between graphene and POPC bilayers. Recently, the same model of graphene was used to simulate its interaction with the DPPC monolayer.[44,57] Considering that the SWCNT has the same atomic structure as graphene, our simulations of interactions between SWCNTs and PSM should obtain accurate results using current CG models.

Simulation details

The MARTINI force field[58] was used for all simulations. Compared with the AA model, the CG models map a group of atoms into one interaction site and thus allow simulations to be carried out on a larger length scale and a longer time scale. Each simulation started with two SWCNTs under vacuum above and below the pre-equilibrated PSM. After energy minimization, the CGMD simulations with constant particle number, surface tension and temperature were carried out. In all simulations, a cutoff of 1.2 nm was used for van der Waals interactions. The Lennard–Jones potential was smoothly shifted to zero between 0.9 nm and 1.2 nm to reduce the cutoff noise. The Coulomb potential, with a cutoff of 1.2 nm, was smoothly shifted to zero from 0 nm to 1.2 nm. The temperature was kept at 310 K by using the Berendsen weak coupling algorithm with a time constant of 2.5 ps. The surface tension, which is given by the formula: $\gamma_{\text{m}} = (P_z - P_{xy})L_z/2$, was kept constant at 10 mN m^{-1} and 30 mN m^{-1}, under which the PSM is considered to exist in the compressed state and the expanded state, respectively.[59] The normal pressure for the z-direction was kept at 1.0 bar. The compressibility in the x–y plane, which is defined as $\beta = -\frac{1}{A}\frac{\partial A}{\partial P_{xy}}$, was set at 5 × 10^{-5} bar^{-1}. The size of the box normal to the membrane was kept a constant by setting the compressibility in the normal direction at 0 bar^{-1}. The neighboring list for non-bonded interactions was updated every 10 steps. All simulations were performed using GROMACS 4.6.7.[60] Snapshots of the simulation system were taken using VMD.[61]

Results and discussion

At present, it is possible to synthesize SWCNTs with specified sizes for their practical applications,[62,63] while the size distribution of SWCNTs is generally polydisperse. SWCNTs with random size distribution can also be produced *via* incomplete combustion of fossil fuels.[64] Here, SWCNTs with diameter d ranging from 1.76 nm to 7.04 nm and length l ranging from 1.25 nm to 18.82 nm were constructed (Fig. S1c†). Two PSM configurations with surface tensions of 30 mN m^{-1} and

10 mN m^{-1} were prepared to model, respectively, the conditions of inspiration and expiration.[54]

SWCNT size modulates its interaction with PSM

Since inhaled SWCNTs attack the PSM most probably during inspiration, we first studied the SWCNT–PSM interaction under a surface tension of 30 mN m^{-1}.[59] 24 independent simulations were performed to determine the molecular mechanisms and kinetics behaviors of SWCNTs interacting with the PSM. Representative interaction pathways are summarized in Fig. 1a and b, which provide the typical snapshots as well as a phase diagram of the interaction states on the d–l plane. As indicated in Fig. 1b, the phase diagram is divided into four characteristic regions according to the interaction states and kinetic pathways.

First, regarding short SWCNTs with lengths comparable to the monolayer thickness, they were found to vertically insert into the PSM (Fig. 1). The difference is that ultrashort SWCNTs (l < 2 nm) simply inserted into the PSM with no indication of PSM perturbation, while a little bit longer SWCNTs (2 nm < l < 6 nm) opened water pores *via* lipid rearrangement inside the tubes if d > 3 nm. This indicates severe perturbation on the PSM ultrastructure. Thinner SWCNTs (d < 2 nm) simply lay down and were immersed in the PSM, being well covered by adjacent lipid tails. By increasing the tube diameter and length (d > 3 nm and l > 6 nm), a more severe PSM perturbation was induced *via* lipid rearrangement both inside and outside the tube. To increase the contact area with SWCNTs in horizontal alignment, adjacent lipid molecules diffused to cover the SWCNTs from both the inner and outer sides. Besides, a number of lipids were extracted from the PSM and covered the SWCNTs from the top side by forming inverse micelles.

During expiration, the PSM undergoes a transition from the expanded state to the compressed state,[59] and buckling or even collapse may take place under PSM compression.[52] By fixing the surface tension of the PSM at 10 mN m^{-1}, we investigated the SWCNT–PSM interaction under compression. Five typical interaction states were identified and shown in Fig. 1c and d. Indeed, they are quite different from those under PSM expansion (30 mN m^{-1}), and the differences, again, strongly depend on the tube size. First, for ultrashort SWCNTs (l < 2 nm), they inserted vertically into the PSM with no indication of either PSM perturbation or translocation, just like that

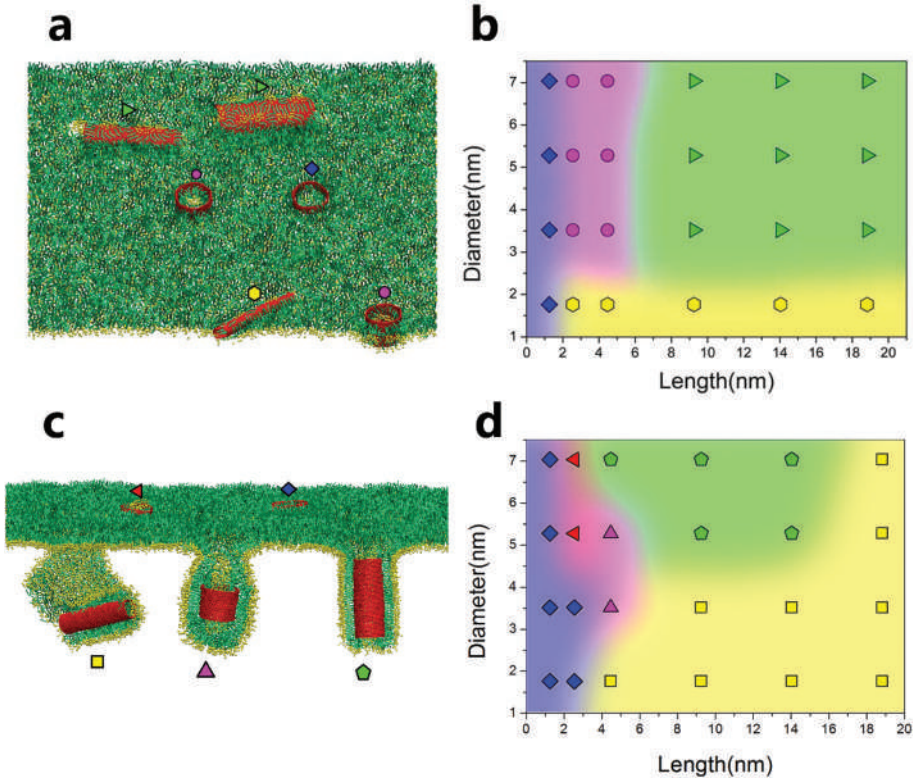

Fig. 1 Typical states for the interaction between SWCNTs and PSM (a, c) and the corresponding phase diagrams (b, d) under both inspiration and expiration conditions. The surface tensions of PSM were set at 30 mN m^{-1} and 10 mN m^{-1}, under which the PSM exhibits the expanded state (a, b) and the compressed state (c, d). The tube diameter ranges from 1.76 nm to 7.04 nm and the tube length varies from 1.25 nm to 18.82 nm. In the phase diagrams, symbols are colored and grouped according to the states. Under inspiration conditions (b): (blue rhombus) vertical insertion, (purple circle) vertical insertion with a PSM pore, (yellow hexagon) PSM insertion with horizontal alignment, (green triangle) horizontal insertion with lipid extraction and inverse micelle assembly; under expiration conditions (d): (blue rhombus) vertical insertion, (red triangle) vertical insertion with lipid extraction, (purple triangle) SWCNT encapsulation by PSM vesiculation, (yellow square) translocation with horizontal alignment, (green pentagon) translocation with an entry angle of 90°.

under PSM expansion. This behavior indicates that the inhaled ultrashort SWCNTs are hard to remove from the monolayer, possibly leading to their accumulation in the PSM and hence causing prolonged retention and increased inflammation potentials. Interestingly, a small increase of tube length could result in an obvious PSM perturbation (2 nm < l < 4 nm and d > 5 nm). Due to the mismatch between tube length and monolayer thickness, several lipid molecules were extracted from the PSM and adsorbed onto the end of the SWCNT. In this case, the water channel formed during inspiration was blocked. With a further increase of tube length, the translocation of SWCNTs can be accomplished *via* shape transformation of PSM under compression. Specifically, SWCNTs with both a length and diameter of about 3–5 nm were finally encapsulated *via* PSM vesiculation and/or folding. Regarding longer and thinner SWCNTs, they were wrapped by the PSM *via* transforming from monolayer into bilayer. This state occupies the right bottom of the diagram and becomes terraced narrower when the diameter increases. With the same length but increasing diameter, the SWCNTs were wrapped by the PSM with an entry angle of 90°.

Vertical insertion and PSM pore formation

It has been observed that under PSM expansion (30 mN m^{-1}), short SWCNTs (l < 5 nm) inserted vertically into PSM and kept standing during the simulations (Fig. 1a and b). The vertical insertion not only maximizes the interaction with lipid tails, but also reduces the PSM perturbation compared with horizontal alignment. Nevertheless, the PSM perturbation by short SWCNTs should not be neglected. Fig. 2a–h shows the typical snapshots from both the top and cross sectional views to illustrate PSM perturbation by SWCNTs with the fixed diameter of 5.28 nm and lengths of 1.28 nm, 2.55 nm and 4.47 nm, respectively. The local structure of the PSM in the absence of the SWCNT was also provided as a reference (Fig. 2a and e). The order parameter that represents the molecular orientation of lipids is generally used to reflect the phase transition and coexistence of the PSM.[59,65] To quantitatively compare both the nature and extent of lipid rearrangement both inside and outside the tube, the order parameter diagram of lipid molecules, $S = \left\langle \frac{1}{2}(3\cos^2\theta_n - 1) \right\rangle$, is provided in Fig. 2i–l, where θ_n is the angle between the bond connecting two adjacent tail beads and the PSM normal (Fig. S2†).[54] Considering that both lipids and SWCNTs keep diffusing in the PSM during the simulation, the order parameter for each lipid was calculated according to the final structure rather than averaged over time.[41]

Our simulations showed that the PSM perturbation by lipid rearrangement around SWCNTs is strongly dependent on the tube length. For an ultrashort SWCNT (l = 1.28 nm), no apparent lipid rearrangement was observed (Fig. 2b and f). The negligible PSM perturbation is also demonstrated in Fig. 2j which shows a homogeneous distribution of the lipid order parameter, similar to the PSM in the absence of the SWCNT

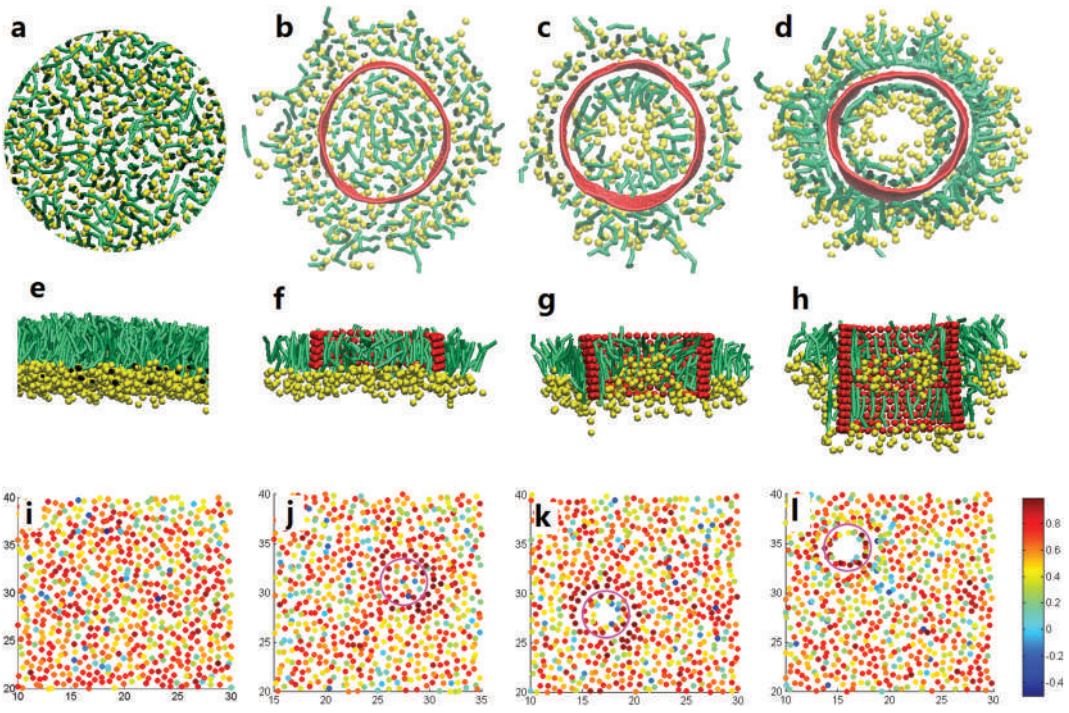

Fig. 2 Vertical insertion of short SWCNTs with length dependent PSM perturbation: (a–d) the local configuration from the top view; (e–h) the local configuration from the cross sectional view; (i–l) the corresponding diagram showing the order parameter of each lipid molecule. The PSM surface tension was set at 30 mN m^{-1}, and the tube diameter was set at 5.28 nm. The local structure of PSM in the absence of SWCNTs is provided for comparison (a, e, i). The tube length was set at 1.28 nm (b, f, j), 2.55 nm (e, g, k) and 4.47 nm (d, h, l), respectively. The locations of SWCNTs are marked by red circles in the diagrams.

(Fig. 2i). For the SWCNT with a length of 2.55 nm, the lipid molecules appear to undergo rearrangement inside the tube (Fig. 2c, g and k). This perturbation is more evident for the SWCNT with a length of 4.47 nm (Fig. 2d, h and l). The blank area in the order parameter diagram suggests that a water pore has formed inside the tube. For lipids adjacent to the pore, the higher order parameter suggests that they adhered on the inner tube surface to increase their contact area, while in the area away from the SWCNT, the order parameters follow a normal composite distribution, indicating that short SWCNTs affect the phase behavior of the PSM significantly only in the local range. We interpret that the lipid rearrangement inside SWCNTs is ascribed to the mismatch between the tube length and monolayer thickness. To increase the contact area between lipids and SWCNTs (Fig. S3†), lipids inside the tubes reassembled with tails adhering onto the inner tube surface and heads pointing towards the water channel.

Despite the fact that the PSM perturbation by inserting short SWCNTs is reduced *via* vertical alignment, potential toxicity exists due to the formation of water pores throughout the monolayer. We monitored the number of water molecules escaping from the monolayer both with and without water pores. It appears that the extent of water leakage was enhanced by opening of water pores (Fig. S4†). Besides, the opened water pore was found to be stable during the simulation, even under further compression of the PSM (Fig. S5†). This indicates that the destructive PSM poration on insertion of SWCNTs might be lasting. By comparing the area of the PSM inserted by a short SWCNT with that of the pure PSM under different tensions, we found that PSM compression is strongly inhibited by inserting short SWCNTs (Fig. S5†). We ascribe the mechanical inhibition to lipids inside the SWCNT, which are separated from those at the PSM and are immune to the outer compression. This is an important indication of biophysical inhibition.

Lipid extraction and inverse micelle assembly

Longer SWCNTs were found to insert into PSM with horizontal alignment. The final snapshots are shown in Fig. 3, which reveals the diameter dependent interactions. Clearly, a thinner SWCNT (d = 1.76 nm) was simply immersed in the PSM with slight PSM perturbation (Fig. 3a). With the increase of tube diameter, a severe PSM perturbation was observed. Specifically, a number of lipid molecules were extracted from the PSM and assembled into inverse micelles to adsorb onto the SWCNT from the top side, indicating lipid depletion from the PSM (Fig. 3b–d). Fig. 3e shows that the number of extracted lipids increased roughly linearly with the tube diameter. Accordingly, the monolayer area of the PSM decreased with the tube diameter, indicating enhanced PSM perturbation with increasing the tube diameter (Fig. 3e). In fact, lipid molecules can also be extracted from cell membranes by carbon nanoparticles, like graphene and SWCNTs.[22,66,67] In the pulmonary system, similarly, the lipid extraction from PSM would cause severe lipid deficiency and thus disturb its biophysical properties.

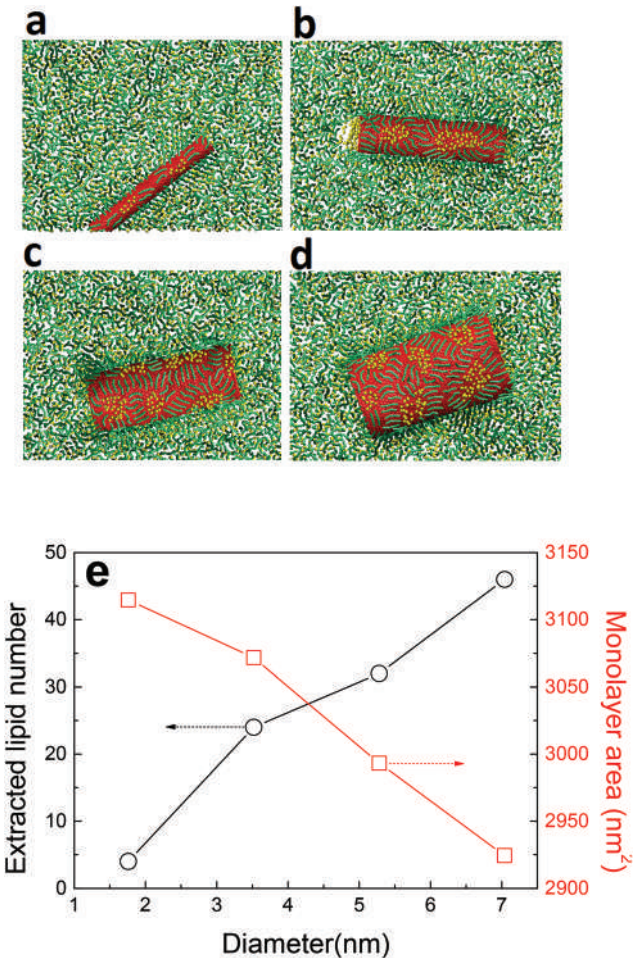

Fig. 3 Insertion of SWCNTs into PSM with lipid extractions and inverse micelle assembly. Figures (a–d) show the local configurations, showing the diameter dependent interaction states, and figure (e) gives the number of extracted lipids and corresponding lipid area as a function of tube diameter, revealing the enhanced PSM perturbation by the increase of tube diameter. The PSM surface tension is fixed at 30 mN m^{-1}. The tube length is 14.04 nm, and the tube diameter varies from 1.76 nm (a) to 3.52 nm (b), 5.28 nm (c) and 7.04 nm (d).

Lipid extraction could be one potential source of the pulmonary nanotoxicity, especially for long SWCNTs. In addition, for long SWCNTs, *e.g.* longer than 20 nm, the nanotoxicity could also come from the rigidifying effect of SWCNTs: the long SWCNTs rigidify locally a region of the monolayer larger than the domain area they covered, as demonstrated for graphene nanosheets.[44] To measure the rigidifying effect, we calculated the area of the PSM deposited with a longer SWCNT (l = 18.82 nm) and compared it with that of the pure PSM (Fig. S6†). The sudden decrease of the monolayer area indicates a phase transition for the pure PSM, while compression for the PSM deposited with a long SWCNT is inhibited. This means that once a number of long SWCNTs adhere onto the PSM surface, expiration or PSM compression will be strongly affected, thus likely leading to respiratory failure.

To visualize how SWCNTs insert into PSM and extract lipids from the PSM, the time sequence of typical snapshots as well as the time evolutions of both the SWCNT–PSM distance and the angle between them are given in Fig. 4 (for more details, see Video S1†). The tube diameter and tube length were set at 5.28 nm and 14.04 nm, respectively. Before deposition, the SWCNT first translated and rotated freely under vacuum (Fig. 4a, t < 1.5 ns). Shortly afterwards, it came into contact with the PSM with a finite attack angle (t = 1.5 ns). To increase the contact area with PSM, it rapidly lay down on the PSM surface, corresponding to a sudden increase of angle between the tube axis and the PSM surface (Fig. 4b). Subsequently, the SWCNT was immersed in PSM, with lipids adhering on the tube surface to prevent its exposure to both water and vacuum. In Fig. 4c, we counted the number of lipids in contact with both the inner and outer surfaces of the SWCNT. Apparently, once deposited (t = 1.5 ns), adjacent lipids started to cover the SWCNT from both sides rapidly and synchronously, confirming that both the exterior and interior of SWCNTs contribute to their insertion into the PSM.

To illustrate the distinct lipid rearrangements inside and outside the tube, the final snapshots from different views are given in Fig. S7.† First, from the top view, the lipid molecules extracted from the PSM assembled into inverse micelles on the outer surface of the SWCNT with heads clustering into several patches and tails covering the tube cooperatively (Fig. S7a†). The inverse micelle assembly is ascribed to the unfavorable exposure of lipid headgroups under vacuum, and this specific arrangement maximizes the interaction between the lipids and the SWCNT. Comparatively, adjacent lipids in the plane of PSM were less perturbed (Fig. S7b†), while those beneath the tube protected it from water by forming the semi-cylindrical micelle (Fig. S7c†). There were also some lipid molecules diffusing to cover the inner tube surface. From the sectional view, lipids inside the tube arranged with tails attached on the inner surface and heads pointing inside, leaving a narrow channel filled with water molecules (Fig. S7d†). This composite structure indicates that this kind of SWCNT could be used as drug carriers for translocation across the PSM. Similar lipid arrangement and water pore formation inside SWCNTs were previously reported by Lelimousin and Sansom when investigating the insertion of SWCNTs into a cell membrane.[21]

Competition between SWCNT rotation and PSM invagination determines the final entry angle

Under the conditions of expiration, longer SWCNTs (l > 6 nm) were found to accomplish translocation *via* shape transformation of PSM (Fig. 1c). We chose the SWCNT with a length of

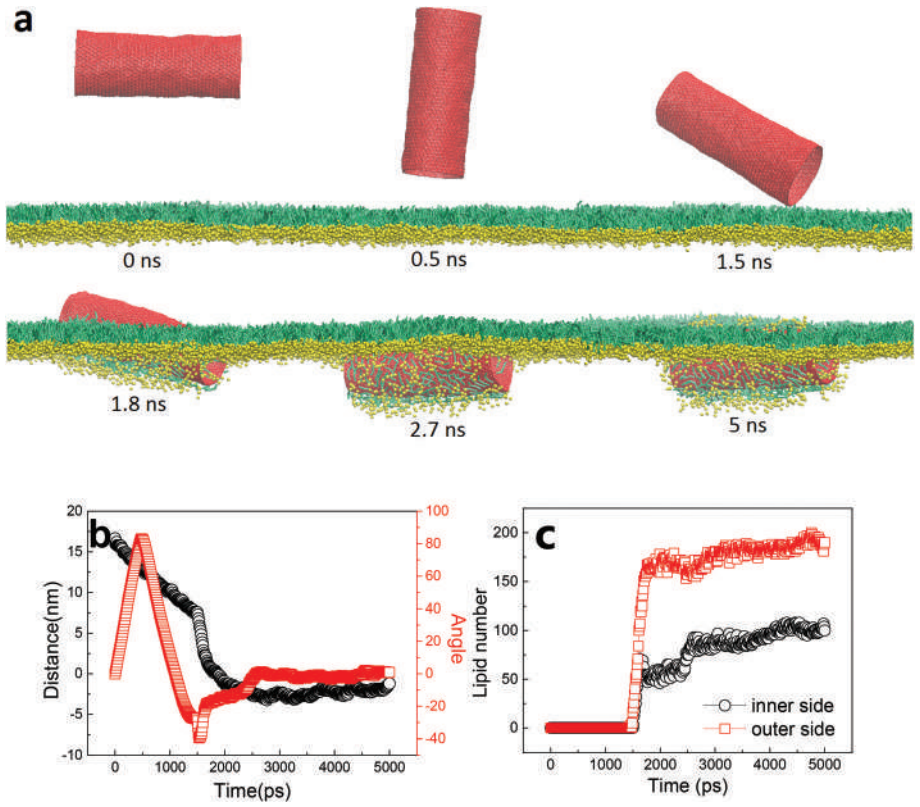

Fig. 4 Insertion of SWCNTs into PSM: figure (a) gives the time sequence of typical snapshots; (b) the time evolution of the distance between the center of SWCNTs and the PSM and that of the angle between the tube axis and the PSM surface; (c) the number of lipids attached on both the inner and outer surfaces of SWCNTs. The tube diameter and tube length are 5.28 nm and 14.04 nm. The PSM surface tension is 30 mN m^{-1}. Water molecules are omitted for clarity.

14.04 nm and a diameter of 3.52 nm to investigate the translocation process (Video S2†). According to Fig. 5, the translocation process can be roughly divided into several stages. The first stage was characterized by random translation and rotation under vacuum (Fig. 5a, t < 0.5 ns). Once captured by the PSM in a finite attack angle, the SWCNT quickly lay down to increase the contact area with PSM (t = 1 ns). The transient rotation was reflected by a sudden decrease of angle between the tube axis and the PSM surface (Fig. 5b, t < 5 ns). When the most segment of the SWCNT was immersed in PSM, a second rotation of the SWCNT towards vertical alignment was captured (see the increase of angle at 5–10 ns in Fig. 4b). We ascribe the rotation to reducing the asymmetric elastic strain of the bending PSM around the tilted SWCNT.[23,68] Nevertheless, the fast PSM invagination under compression prevented the SWCNT from further rotating. Afterwards, the tilt angle of the SWCNT reached equilibrium at the value of 40° for 20 ns, until a third rotation attempt occurred before detaching from the PSM (t = 40 ns). However, the detachment of the SWCNT was achieved *via* formation of the bilayer neck that connects the SWCNT with the PSM. Finally, the wrapped SWCNT rotated gradually back to horizontal alignment and kept moving downwards under PSM compression in the rest of the simulation.

With the same length but increasing diameter, surprisingly, the SWCNT finally stood up and was completely wrapped by the PSM (Fig. 1c), similar to its interactions with lipid bilayers.[23] Clearly, increasing tube diameter results in a distinct pathway of interaction between the SWCNT and PSM (Fig. 6 and Video S3†). As shown in Fig. 6a, the entry of the SWCNT with the diameter of 5.28 nm is featured with a wrapping–rotation mechanism.[69] Upon deposition, the SWCNT first lay down to increase the contact area with the PSM. Meanwhile, the PSM bent downwards and wrapped the SWCNT in an endocytic pathway. Due to the anisotropic shape, the invagination of the SWCNT with a finite tilt angle resulted in an asymmetric elastic strain of the bending PSM around it. To reduce the bending asymmetry, the SWCNT kept rotating and finally achieved an entry angle close to 90° (Fig. 6b). The top view of the final configuration clearly shows the regular and symmetric arrangement of lipids standing on the outer surface of the SWCNT, while those inside the tube adhered on the inner surface, leaving a narrow porous channel filled with water molecules (Fig. 6c). To check the

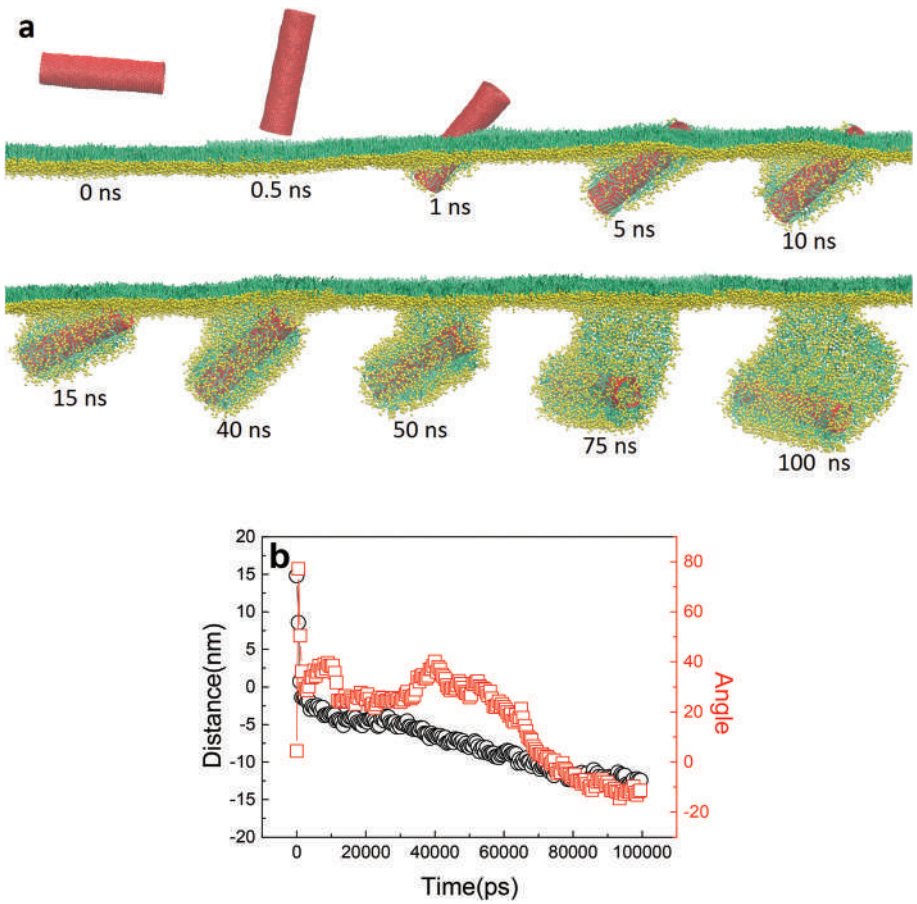

Fig. 5 Efficient PSM translocation of SWCNTs with a diameter of 3.52 nm and a length of 14.04 nm. Figure (a) shows the time sequence of typical snapshots, revealing the detailed translocation pathway with self-rotation; figure (b) gives the time evolutions of the distance between the tube center and the PSM and that of the angle between the tube axis and the PSM surface. The PSM surface tension is set at 10 mN m^{-1}.

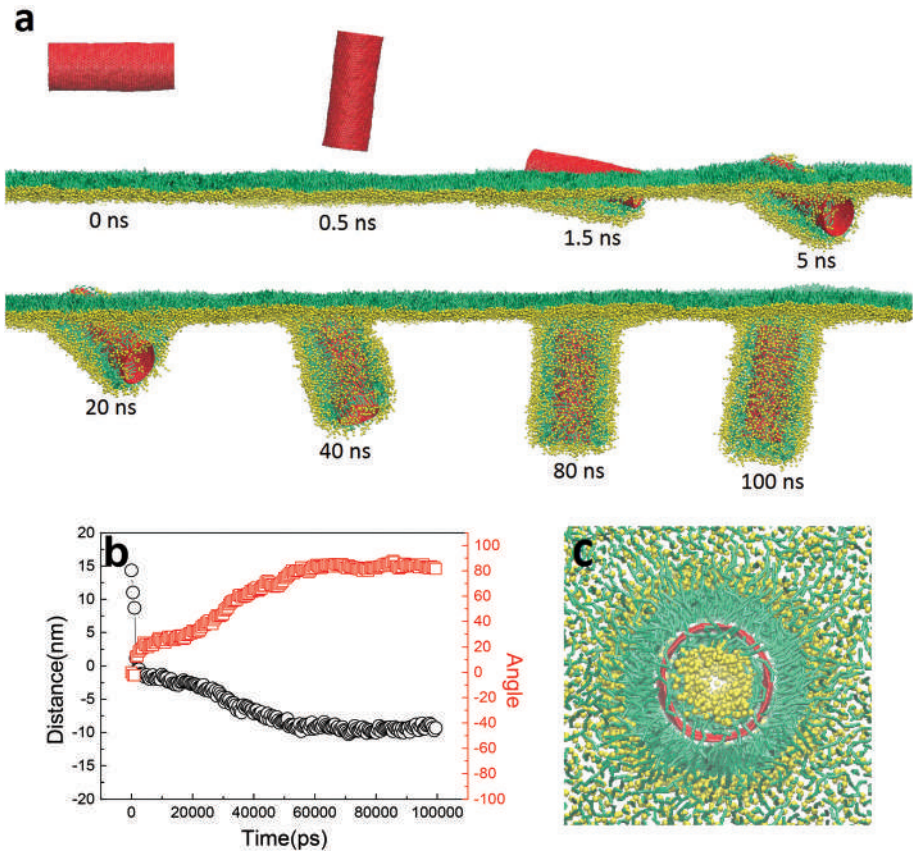

Fig. 6 PSM wrapping of SWCNTs with a final entry angle of 90°: (a) the typical snapshots illustrating the detailed PSM wrapping with SWCNT rotation; (b) the evolution of the tube position along the *z* direction and that of the angle between the tube axis and the PSM surface; (c) the local configuration from the bottom view, illustrating the regular arrangement of lipids attached on the outer surface of SWCNTs, and the formation of water channels inside the tube. The tube diameter and tube length are 5.28 nm and 14.04 nm. The PSM surface tension is 10 mN m^{-1}.

results, we launched five independent MD simulations starting from the same initial configuration but with different initial velocity distributions. As expected, all simulations showed similar behaviors of SWCNT rotation during PSM wrapping.

Based on the previous modeling of membrane wrapping of nonspherical nanoparticles.[23,69–75] we infer that the asymmetric elastic strain of the bending PSM provides the driving force for rotation of the SWCNT, which minimizes the elastic energy. To test this hypothesis, one restrained MD simulation was performed. The configuration of the SWCNT with a diameter of 3.52 nm and a length of 14.04 nm at t = 10 ns was chosen as the initial structure (Fig. 5a). During the simulation an extra spring force along the z direction with a constant of 1000 kJ mol^{-1} nm^{-2} was exerted on the center of mass of the SWCNT towards the box center. The pulling velocity was set at zero to restrain the SWCNT from further invagination, thus providing sufficient time for it to adjust its orientation. As expected, the tilted SWCNT gradually stood up rather than lay down on the PSM (Fig. S8, Video S4†). Despite the fact that a final entry angle of 90° is energetically favorable due to the minimized elastic energy of the PSM, in reality, the speed of PSM invagination can be altered by varying the surface tension of the PSM. We fixed the tube diameter at 5.28 nm and gradually increased the surface tension of the PSM from 5 mN m^{-1} to 30 mN m^{-1}. Indeed, the final entry angle of the SWCNT is regulated by the surface tension (Fig. S9†). Under surface tension below 10 mN m^{-1}, the PSM becomes unstable at the air–water interface and easily undergoes shape transformation to wrap the SWCNT. The efficient wrapping restrains the SWCNT from rotation to adopt a 90° entry pathway (Fig. 7). Under the intermediate tension of about 10 mN m^{-1}, the invagination is slowed down, thus leaving enough time for the SWCNT to rotate toward the vertical alignment. By further increasing the surface tension, however, the SWCNT was only partially wrapped by the PSM in a horizontal alignment. Besides, lipids were extracted from the PSM and assembled into inverse micelles adsorbing on the top surface of the SWCNT. Both inefficient wrapping and lipid extraction restrain the SWCNT from rotating. We thus conclude that the steady-state entry angle is determined by competition between the speed of tube rotation and that of PSM invagination. Once the former dominates, the SWCNT will adopt a 90° entry pathway. Otherwise, the SWCNT will adopt a smaller entry angle and be efficiently wrapped by the PSM *via* buckling or folding of the monolayer.

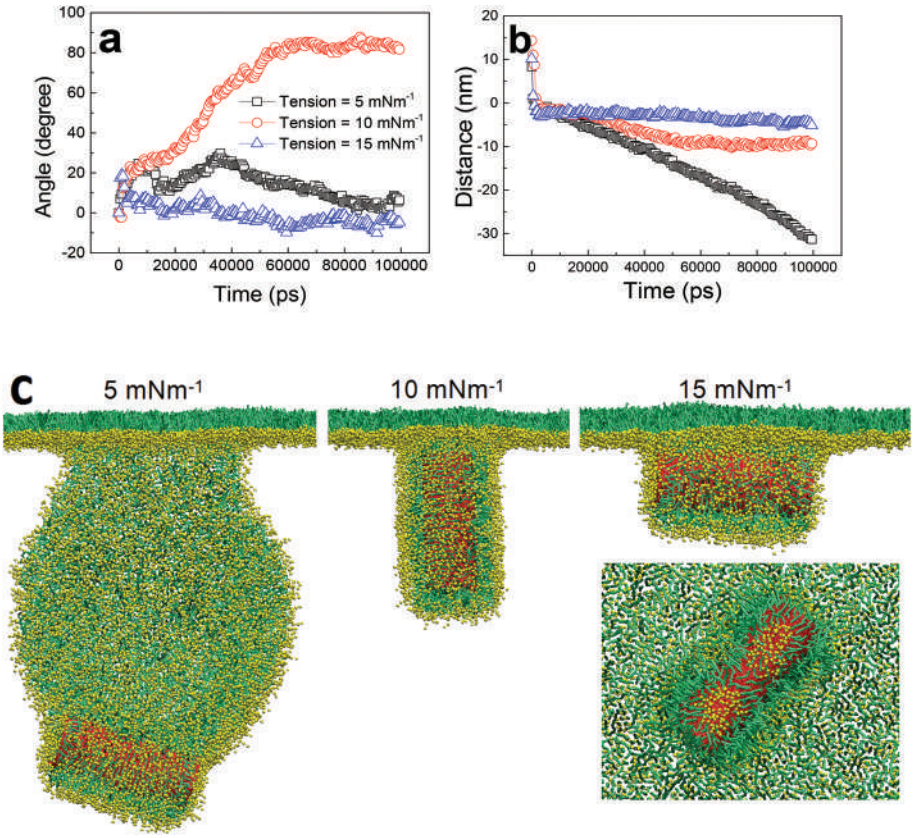

Fig. 7 PSM tension regulates the translocation pathway of SWCNTs with a defined entry angle: (a) the time evolution of the angle between the tube axis and the PSM plane; (b) the time evolution of the distance between the center of SWCNTs and PSM; (c) the final snapshots, illustrating the translocation state. The tube diameter and tube length are 5.28 nm and 14.04 nm.

Vesiculation of the PSM to encapsulate short SWCNTs

Finally, we study the pulmonary entry of short SWCNTs. Similar to inspiration, ultrashort SWCNTs (l = 1.28 nm) vertically inserted into the PSM with no indication of translocation under expiration (Fig. S10a and b†). However, longer SWCNTs (l = 2.55 nm) were found to extract lipids to cover the top end from exposure to vacuum (Fig. S10c and d†). As we increased its length to 4.47 nm, the SWCNT still stood in the PSM, but interestingly, the induced PSM configuration was more like a vesicle (Fig. 1c and Video S5†). Fig. 8a shows that the early invagination completed *via* a wrapping-rotation mechanism (t < 50 ns). In this process both the inner and outer surfaces of the SWCNT were covered by lipid molecules with different arrangements. The bottom end allowed water to diffuse inside the tube, thus creating a hydrophilic environment (Fig. 8b). After invagination with an angle of 90° (t = 50 ns), the wrapping did not terminate but continued to develop into a new configuration. As the simulation proceeded, more lipid molecules were found to accumulate beneath the SWCNT and closed the mouth. Consequently, the PSM invagination gradually grew into a vesicle configuration. Finally, the SWCNT detached from the PSM and was encapsulated in the cavity of newly formed vesicles. The detailed lipid arrangement with encapsulated SWCNTs is clarified by the sectional view in Fig. 8c.

Implications to inhalation toxicity and pulmonary drug delivery

Our simulations have implications for understanding the inhalation toxicity of SWCNTs. Since the PSM forms the first biological barrier against inhaled particles, the perturbation of PSM by SWCNTs should contribute to the observed toxicity of SWCNTs in the respiratory system. In addition, the detailed interaction pathway influences the subsequent fate of SWCNTs once inhaled. For example, incubating NPs with natural PS was found to trigger NP phagocytosis, and even alter the biodistribution of NPs translocated into secondary organs.[76] Previous experiments have shown that increasing the length of SWCNTs results in increased toxicity.[77] Consistently, our simulations demonstrate that longer SWCNTs can induce more severe PSM perturbation *via* lipid rearrangement, lipid depletion and PSM-rigidifying effects. For short SWCNTs, our simulations showed that they vertically insert into the PSM regardless of the surface tension. This may cause toxicological effects. Firstly and most importantly, the inhaled ultrashort SWCNTs are hard to remove from the PSM, thus leading to

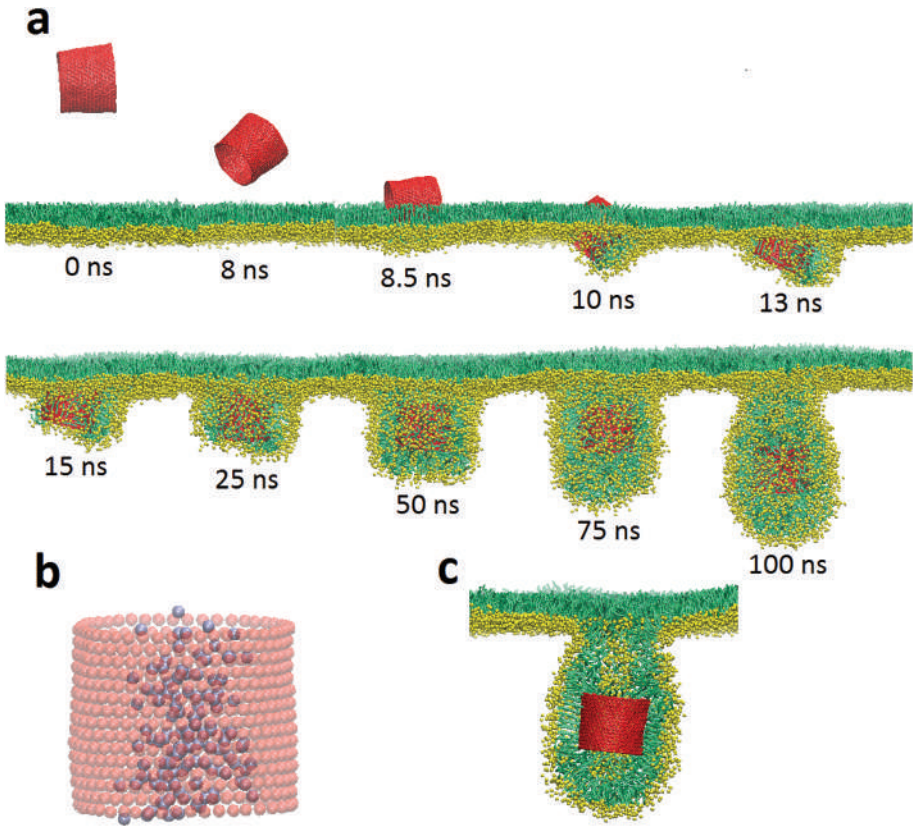

Fig. 8 PSM wrapping with subsequent vesiculation to encapsulate the SWCNT: (a) the time sequence of typical snapshots; (b) SWCNT configuration with the water molecules inside; (c) the sectional view of local configuration, illustrating the detailed lipid arrangement covering the SWCNT. The tube diameter and tube length are 5.28 nm and 4.47 nm. The PSM tension is 10 mN m^{-1}.

their accumulation in PSM with prolonged retention and increased inflammation potentials. In fact, it has been demonstrated that inhaled SWCNTs have prolonged lifetime in the lungs and induce inflammation by forming aggregates in the alveoli.[78,79] Therefore, our simulations may provide a possible molecular mechanism underlying the observed inflammatory response to SWCNTs. Secondly, once inserted into the PSM with vertical alignment, short SWCNTs with a larger tube diameter could induce water pores in the PSM (Fig. 2). In fact, similar behavior of pore formation for PSM was also observed for deposited graphene oxide, but with a rather different mechanism.[57] Here, we relate this effect to that of antimicrobial peptides, which are thought to embed into the membrane and generate a pore-like structure that kills the target. Thirdly, after inserting into PSM, lipids inside the tubes are apparently separated from the outer phase, which is expected to increase the compressibility of the PSM. Notably, this may lead to respiratory failure and is an important indication of biophysical inhibition.

On the positive side, as short SWCNTs vertically insert into PSM with no indication of translocation, a stable SWCNT–PSM composite may be formed by creating water channels inside the short SWCNTs. Importantly, insertion of the short SWCNTs into the PSM allowed them to create an interface that mimics transport in biological pores. Despite the extremely simple structure, these pores could reproduce the major functional behavior of biological channels, such as selective transport of water, ions, and small molecules, *via* carefully changing the tube diameter and length. Our simulations can also help develop SWCNT-based pulmonary drug delivery. As shown by our simulations, longer SWCNTs can accomplish PSM translocation under compression. During translocation, lipid molecules assemble into inverse micelles inside the tube. This may enable the use of longer SWCNTs as drug delivery vehicles by providing a means of encapsulation of drugs. Furthermore, the final entry angle of SWCNTs under PSM compression can be modulated to achieve a desired value, which strongly depends on the tube diameter (see Fig. 1d). In addition to the size of synthesized SWCNTs, in reality, we can intentionally alter the expiration speed to modulate the competition between tube rotation and PSM invagination. Therefore, both the entry efficiency and drug loading capacity of SWCNTs can be increased.

Conclusions

In summary, we have presented a simulation study of the interaction between inhaled SWCNTs and PSM, focusing on the perturbation of PSM by SWCNTs, the formed composite struc-

ture and the PSM translocation of SWCNTs that are modulated by the tube size and PSM tension. Ultrashort SWCNTs vertically insert into the PSM, with no indication of translocation regardless of PSM tension. Thus, stable SWCNT–PSM composites are formed, creating a porous interface that mimics transport in biological channels. The vertical PSM insertion of short SWCNTs implies potential inhalation toxicity from three aspects. First, the inserting ultrashort SWCNTs are hard to remove from PSM, thus leading to their accumulation and causing permanent lung damage; lipid rearrangement inside SWCNTs generates water pores across the monolayer; the PSM compressibility is increased by segregating inner lipids from the outer phase. For longer SWCNTs, they inserted into the PSM with horizontal alignment under expansion. The PSM perturbation is induced *via* lipid rearrangements inside and outside the tubes. Under compression, they can be wrapped through rotation that is driven by asymmetric elastic strain of the bending PSM. The final entry angle is sensitive to tube diameter and determined by the relative timescales for tube rotation and PSM invagination. For much longer SWCNTs, the nanotoxicity could come from both lipid depletion and the PSM-rigidifying effect. We hope that this study can help develop effective strategies against the inhalation toxicity of SWCNTs, and provide guidelines for the use of SWCNTs as pulmonary drug delivery vehicles.

Acknowledgements

This work was financially supported by the National Natural Science Foundation of China (no. 21303269), Science and Technology Major Project of Shandong Province (2016GSF117033), and Qingdao Science and Technology Project (no. 16-5-1-73-jch).

References

1 R. H. Baughman, A. A. Zakhidov and W. A. de Heer, *Science*, 2002, **297**, 787–792.
2 M. F. De Volder, S. H. Tawfick, R. H. Baughman and A. J. Hart, *Science*, 2013, **339**, 535–539.
3 C. W. Lam, J. T. James, R. McCluskey, S. Arepalli and R. L. Hunter, *Crit. Rev. Toxicol.*, 2006, **36**, 189–217.
4 S. Lanone, P. Andujar, A. Kermanizadeh and J. Boczkowski, *Adv. Drug Delivert. Rev.*, 2013, **65**, 2063–2069.
5 V. Castranova, P. A. Schulte and R. D. Zumwalde, *Acc. Chem. Res.*, 2012, **46**, 642–649.
6 K. Kostarelos, A. Bianco and M. Prato, *Nat. Nanotechnol.*, 2009, **4**, 627–633.
7 Z. Liu, S. Tabakman, K. Welsher and H. Dai, *Nano Res.*, 2009, **2**, 85–120.
8 X. Xue, L.-R. Wang, Y. Sato, Y. Jiang, M. Berg, D.-S. Yang, R. A. Nixon and X.-J. Liang, *Nano Lett.*, 2014, **14**, 5110–5117.
9 X. Ma, L.-H. Zhang, L.-R. Wang, X. Xue, J.-H. Sun, Y. Wu, G. Zou, X. Wu, P. C. Wang and W. G. Wamer, *ACS Nano*, 2012, **6**, 10486–10496.
10 Z. Liu, K. Yang and S.-T. Lee, *J. Mater. Chem.*, 2011, **21**, 586–598.
11 N. W. Shi Kam, T. C. Jessop, P. A. Wender and H. Dai, *J. Am. Chem. Soc.*, 2004, **126**, 6850–6851.
12 Q. Lu, J. M. Moore, G. Huang, A. S. Mount, A. M. Rao, L. L. Larcom and P. C. Ke, *Nano Lett.*, 2004, **4**, 2473–2477.
13 D. Pantarotto, J.-P. Briand, M. Prato and A. Bianco, *Chem. Commun.*, 2004, 16–17.
14 C. W. Lam, J. T. James, R. McCluskey and R. L. Hunter, *Toxicol. Sci.*, 2004, **77**, 126–134.
15 J. Melbourne, A. Clancy, J. Seiffert, J. Skepper, T. D. Tetley, M. S. Shaffer and A. Porter, *Biomaterials*, 2015, **55**, 24–32.
16 Y. Zhao, G. Xing and Z. Chai, *Nat. Nanotechnol.*, 2008, **3**, 191–192.
17 A. Bianco, K. Kostarelos, C. D. Partidos and M. Prato, *Chem. Commun.*, 2005, 571–577.
18 C. Ge, J. Du, L. Zhao, L. Wang, Y. Liu, D. Li, Y. Yang, R. Zhou, Y. Zhao, Z. Chai and C. Chen, *Proc. Natl. Acad. Sci. U. S. A.*, 2011, **108**, 16968–16973.
19 A. E. Nel, L. Mädler, D. Velegol, T. Xia, E. M. Hoek, P. Somasundaran, F. Klaessig, V. Castranova and M. Thompson, *Nat. Mater.*, 2009, **8**, 543–557.
20 Q. Mu, G. Jiang, L. Chen, H. Zhou, D. Fourches, A. Tropsha and B. Yan, *Chem. Rev.*, 2014, **114**, 7740–7781.
21 M. Lelimousin and M. S. Sansom, *Small*, 2013, **9**, 3639–3646.
22 E. J. Wallace and M. S. Sansom, *Nano Lett.*, 2008, **8**, 2751–2756.
23 X. Shi, A. von dem Bussche, R. H. Hurt, A. B. Kane and H. Gao, *Nat. Nanotechnol.*, 2011, **6**, 714–719.
24 S. Kraszewski, F. Picaud, I. Elhechmi, T. Gharbi and C. Ramseyer, *Carbon*, 2012, **50**, 5301–5308.
25 K. Kostarelos, L. Lacerda, G. Pastorin, W. Wu, S. Wieckowski, J. Luangsivilay, S. Godefroy, D. Pantarotto, J.-P. Briand and S. Muller, *Nat. Nanotechnol.*, 2007, **2**, 108–113.
26 M. Dutt, O. Kuksenok, M. J. Nayhouse, S. R. Little and A. C. Balazs, *ACS Nano*, 2011, **5**, 4769–4782.
27 L. Wang, L. Zhang, X. Xue, G. Ge and X. Liang, *Nanoscale*, 2012, **4**, 3983–3989.
28 G. Zuo, Q. Huang, G. Wei, R. Zhou and H. Fang, *ACS Nano*, 2010, **4**, 7508–7514.
29 Z. Fu, Y. Luo, P. Derreumaux and G. Wei, *Biophys. J.*, 2009, **97**, 1795–1803.
30 K. Yamashita, Y. Yoshioka, K. Higashisaka, Y. Morishita, T. Yoshida, M. Fujimura, H. Kayamuro, H. Nabeshi, T. Yamashita and K. Nagano, *Inflammation*, 2010, **33**, 276–280.
31 H. S. Choi, Y. Ashitate, J. H. Lee, S. H. Kim, A. Matsui, N. Insin, M. G. Bawendi, M. Semmler-Behnke, J. V. Frangioni and A. Tsuda, *Nat. Biotechnol.*, 2010, **28**, 1300–1303.

32 J. Kolosnjaj-Tabi, J. Just, K. B. Hartman, Y. Laoudi, S. Boudjemaa, D. Alloyeau, H. Szwarc, L. J. Wilson and F. Moussa, *EBioMedicine*, 2015, **2**, 1697–1704.
33 M. Griese, *Eur. Respir. J.*, 1999, **13**, 1455–1476.
34 J. Goerke, *Biochim. Biophys. Acta, Mol. Basis Dis.*, 1998, **1408**, 79–89.
35 E. Lopez-Rodriguez and J. Pérez-Gil, *Biochim. Biophys. Acta, Biomembr.*, 2014, **1838**, 1568–1585.
36 F. X. McCormack and J. A. Whitsett, *J. Clin. Invest.*, 2002, **109**, 707–712.
37 J. A. Whitsett and T. E. Weaver, *N. Engl. J. Med.*, 2002, **347**, 2141–2148.
38 Y. Y. Zuo, R. A. Veldhuizen, A. W. Neumann, N. O. Petersen and F. Possmayer, *Biochim. Biophys. Acta, Biomembr.*, 2008, **1778**, 1947–1977.
39 G. Hu, B. Jiao, X. Shi, R. P. Valle, Q. Fan and Y. Y. Zuo, *ACS Nano*, 2013, **7**, 10525–10533.
40 C.-c. Chiu, W. Shinoda, R. H. DeVane and S. O. Nielsen, *Soft Matter*, 2012, **8**, 9610–9616.
41 X. Lin, T. Bai, Y. Y. Zuo and N. Gu, *Nanoscale*, 2014, **6**, 2759–2767.
42 N. Nisoh, M. Karttunen, L. Monticelli and J. Wong-Ekkabut, *RSC Adv.*, 2015, **5**, 11676–11685.
43 J. Barnoud, L. Urbini and L. Monticelli, *J. R. Soc., Interface*, 2015, **12**, 20140931.
44 T. Yue, X. Wang, X. Zhang and F. Huang, *RSC Adv.*, 2015, **5**, 30092–30106.
45 R. P. Valle, T. Wu and Y. Y. Zuo, *ACS Nano*, 2015, **9**, 5413–5421.
46 K. Bhattacharya, F. T. Andon, R. El-Sayed and B. Fadeel, *Adv. Drug Delivery Rev.*, 2013, **65**, 2087–2097.
47 J. P. Ryman-Rasmussen, E. W. Tewksbury, O. R. Moss, M. F. Cesta, B. A. Wong and J. C. Bonner, *Am. J. Respir. Cell Mol. Biol.*, 2009, **40**, 349–358.
48 B. Robertson and H. L. Halliday, *Biochim. Biophys. Acta, Mol. Basis Dis.*, 1998, **1408**, 346–361.
49 J. Wong-Ekkabut, S. Baoukina, W. Triampo, I.-M. Tang, D. P. Tieleman and L. Monticelli, *Nat. Nanotechnol.*, 2008, **3**, 363–368.
50 T. Yue, Y. Xu, S. Li, X. Zhang and F. Huang, *Phys. Chem. Chem. Phys.*, 2016, **18**, 18923–18933.
51 H. m. Ding and Y. q. Ma, *Small*, 2015, **11**, 1055–1071.
52 S. Baoukina, L. Monticelli, H. J. Risselada, S. J. Marrink and D. P. Tieleman, *Proc. Natl. Acad. Sci. U. S. A.*, 2008, **105**, 10803–10808.
53 S. L. Duncan and R. G. Larson, *Biophys. J.*, 2008, **94**, 2965–2986.
54 X. Lin, Y. Li and N. Gu, *Soft Matter*, 2011, **7**, 3882–3888.
55 X. Lin, Y. Y. Zuo and N. Gu, *Sci. China Mater.*, 2015, **58**, 28–37.
56 A. V. Titov, P. Král and R. Pearson, *ACS Nano*, 2009, **4**, 229–234.
57 Q. Hu, B. Jiao, X. Shi, R. P. Valle, Y. Y. Zuo and G. Hu, *Nanoscale*, 2015, **7**, 18025–18029.
58 S. J. Marrink, H. J. Risselada, S. Yefimov, D. P. Tieleman and A. H. De Vries, *J. Phys. Chem. B*, 2007, **111**, 7812–7824.
59 S. Baoukina, L. Monticelli, S. J. Marrink and D. P. Tieleman, *Langmuir*, 2007, **23**, 12617–12623.
60 B. Hess, C. Kutzner, D. Van Der Spoel and E. Lindahl, *J. Chem. Theory Comput.*, 2008, **4**, 435–447.
61 W. Humphrey, A. Dalke and K. Schulten, *J. Mol. Graphics*, 1996, **14**, 33–38.
62 C. L. Cheung, A. Kurtz, H. Park and C. M. Lieber, *J. Phys. Chem. B*, 2002, **106**, 2429–2433.
63 Y. Yang, L. Xie, Z. Chen, M. Liu, T. Zhu and Z. Liu, *Synth. Met.*, 2005, **155**, 455–460.
64 L. Murr, J. Bang, D. Lopez, P. Guerrero, E. Esquivel, A. Choudhuri, M. Subramanya, M. Morandi and A. Holian, *J. Mater. Sci.*, 2004, **39**, 2199–2204.
65 S. Baoukina, E. Mendez-Villuendas and D. P. Tieleman, *J. Am. Chem. Soc.*, 2012, **134**, 17543–17553.
66 Y. Tu, M. Lv, P. Xiu, T. Huynh, M. Zhang, M. Castelli, Z. Liu, Q. Huang, C. Fan and H. Fang, *Nat. Nanotechnol.*, 2013, **8**, 594–601.
67 L. Zhang, B. Xu and X. Wang, *J. Phys. Chem. B*, 2016, **120**, 957–964.
68 X. Yi, X. Shi and H. Gao, *Nano Lett.*, 2014, **14**, 1049–1055.
69 C. Huang, Y. Zhang, H. Yuan, H. Gao and S. Zhang, *Nano Lett.*, 2013, **13**, 4546–4550.
70 Y. Li, T. Yue, K. Yang and X. Zhang, *Biomaterials*, 2012, **33**, 4965–4973.
71 J. Mao, P. Chen, J. Liang, R. Guo and L.-T. Yan, *ACS Nano*, 2016, **10**, 1493–1502.
72 R. Vácha, F. J. Martinez-Veracoechea and D. Frenkel, *Nano Lett.*, 2011, **11**, 5391–5395.
73 S. Dasgupta, T. Auth and G. Gompper, *Nano Lett.*, 2014, **14**, 687–693.
74 K. Yang, B. Yuan and Y.-q. Ma, *Nanoscale*, 2013, **5**, 7998–8006.
75 L. Chen, S. Xiao, H. Zhu, L. Wang and H. Liang, *Soft Matter*, 2016, **12**, 2632–2341.
76 A. A. Kapralov, W. H. Feng, A. A. Amoscato, N. Yanamala, K. Balasubramanian, D. E. Winnica, E. R. Kisin, G. P. Kotchey, P. Gou and L. J. Sparvero, *ACS Nano*, 2012, **6**, 4147–4156.
77 K. Kostarelos, *Nat. Biotechnol.*, 2008, **26**, 774–776.
78 A. A. Shvedova, E. R. Kisin, R. Mercer, A. R. Murray, V. J. Johnson, A. I. Potapovich, Y. Y. Tyurina, O. Gorelik, S. Arepalli and D. Schwegler-Berry, *Am. J. Physiol.: Lung Cell. Mol. Physiol.*, 2005, **289**, L698–L708.
79 C. A. Poland, R. Duffin, I. Kinloch, A. Maynard, W. A. Wallace, A. Seaton, V. Stone, S. Brown, W. MacNee and K. Donaldson, *Nat. Nanotechnol.*, 2008, **3**, 423–428.

